ELSEVIER

Earth and Planetary Science Letters 193 (2001) 437–446

EPSL

www.elsevier.com/locate/epsl

Earthquake cycle dominates contemporary crustal deformation in Central and Southern Andes

Jürgen Klotz [a,*], Giorgi Khazaradze [a], Detlef Angermann [a,1], Christoph Reigber [a], Raul Perdomo [b], Oscar Cifuentes [c]

[a] *GeoForschungsZentrum Potsdam, PB 1.1, Telegrafenberg, 14473 Potsdam, Germany*
[b] *Obs. Astronomico de La Plata, La Plata, Argentina*
[c] *Instituto Geografico Militar, Santiago de Chile, Chile*

Received 28 May 2001; received in revised form 20 September 2001; accepted 24 September 2001

Abstract

With the advent of global positioning system (GPS) technology and its applications to high precision geodesy, earth scientists have gained an unprecedented opportunity to study the kinematics and dynamics of present-day deformation processes along plate boundary zones. However, until now our knowledge of the deformation processes associated with the Andean subduction along the western coast of South America has been limited. Here we present first estimates of present-day crustal deformation rates in the central and southern sections of the Andes, between latitudes 22°S and 42°S. We find that the deformation in the central section of our study area is dominated by the interseismic phase of an earthquake deformation cycle, caused by 100% coupling of the thrust interface between the subducting Nazca and the overriding South America plates. The estimated depth of coupling is not uniform along strike: north of 30°S it is ~33 km deep, while south of 35°S it reaches 50 km depth. In addition, we observed postseismic relaxation effects in the northern part of our network in the area of the 1995 M_w8.0 Antofagasta earthquake. South of 38°S, we detected a similar deformation pattern as in the Antofagasta area which we attribute to postseismic relaxation effects of the 1960 M_w9.5 Valdivia earthquake.

Keywords: Global Positioning System; subduction zones; plate coupling/decoupling; postseismic relaxation; Southern Andes; crustal thickening

1. Introduction

The Andean subduction zone (ASZ) is formed as a result of oblique subduction of the oceanic Nazca plate beneath the continental South America plate. This tectonically active convergent margin stretches along the western coast of South America from Columbia to southern Chile for more than 7500 km and is the longest subduction zone in the world. The Andean tectonics is characterized by prominent along-strike variations [1,2]. From Wadati–Benioff seismicity studies it is known that below 100 km depth the subducting

* Corresponding author. Tel.: +49-331-288-1118; Fax: +49-331-288-1759.
E-mail address: klotz@gfz-potsdam.de (J. Klotz).

[1] Present address: Deutsches Geodätisches Forschungsinstitut, München, Germany.

0012-821X/01/$ – see front matter
PII: S0012-821X(01)00532-5

Table 1
GPS station locations and calculated horizontal velocities

Station ID	Longitude	Latitude	W–E vel. (mm/yr)	1σ error	S–N vel. (mm/yr)	1σ error	Correl. coeff.
1994–1996 campaigns							
ANTU	288.3745	−37.3358	16.4	2.1	1.3	2.0	0.05
AUMA	291.4048	−37.6065	−1.9	1.9	−4.0	2.0	0.01
BARI	288.5865	−41.1321	−11.7	2.0	−3.2	2.2	0.09
BING	289.1413	−27.1341	20.1	2.1	6.0	1.9	−0.07
BOAL	295.4522	−31.5955	−5.7	1.9	−0.1	1.9	−0.05
BSAR	288.5891	−28.8162	17.4	2.1	8.9	1.9	−0.05
BSJL	288.6620	−30.6870	20.0	2.1	9.0	1.9	−0.02
BULN	287.6753	−36.7978	29.5	2.0	2.7	2.0	0.07
CALF	286.6116	−39.7539	16.3	2.0	7.4	2.1	0.12
CANT	294.9295	−35.1193	2.2	1.9	3.3	2.0	−0.05
CART	288.3719	−33.5538	17.9	2.0	7.6	1.9	0.01
CAVI	292.9957	−27.5538	−2.9	1.9	0.6	1.9	−0.05
CCAL	289.1783	−33.6772	19.8	2.0	5.6	1.9	0.01
CCHA	289.3052	−32.9544	19.2	2.0	2.0	1.9	−0.00
CCRE	289.9262	−32.8237	11.7	1.9	−5.2	1.9	−0.01
CECR	293.0510	−29.4242	3.2	2.1	2.5	1.9	−0.04
CEGU	291.5176	−29.5058	4.0	2.0	5.5	1.9	−0.03
CELI	291.1259	−34.4728	3.1	1.9	3.9	1.9	−0.01
CEPI	289.3679	−40.2494	−6.7	2.0	−1.2	2.1	0.07
CERC	290.9353	−30.5882	3.7	1.9	5.0	1.9	−0.03
CEVA	291.4599	−31.8614	3.2	1.9	−0.7	1.9	−0.02
CHAP	289.5001	−29.8529	15.8	2.0	9.6	1.9	−0.03
CHIM	288.9056	−34.7242	21.3	2.1	5.8	2.0	0.02
CHOL	287.5584	−42.0279	−5.8	2.0	0.6	2.2	0.12
CHOS	289.6855	−37.3608	5.9	1.9	−6.7	2.0	0.04
CMOR	289.2037	−30.2054	17.5	1.9	5.9	1.9	−0.03
COMA	289.7824	−41.0363	−9.5	2.0	1.0	2.2	0.06
CONC	289.3740	−31.8929	18.1	2.0	6.8	1.9	−0.02
CONS	287.5851	−35.3180	34.2	2.1	6.4	2.0	0.04
CURA	287.3754	−35.8363	31.5	2.2	8.7	2.0	0.04
ELAL	290.1891	−35.1805	4.1	1.9	3.7	2.0	0.01
ELCH	291.1123	−39.2906	−3.4	1.9	2.5	2.1	0.02
ELSA	290.3688	−26.2450	9.4	2.1	7.3	1.9	−0.07
EPUY	288.5956	−42.1405	−7.6	2.0	0.5	2.2	0.10
ETRA	289.7135	−28.8653	13.5	2.0	8.5	1.9	−0.05
FRIA	294.7195	−28.6265	1.2	1.9	2.8	1.9	−0.04
FTRN[a]	287.6233	−40.1304	−0.3	2.0	8.6	2.1	0.10
GARR	294.8506	−33.6955	−1.0	1.9	2.4	1.9	−0.04
GUAB	285.9728	−41.8063	16.2	2.0	9.2	2.2	0.15
GUAS	295.1758	−28.1365	−5.2	1.9	1.0	1.9	−0.03
LAAM	289.9449	−38.8360	−1.1	1.9	−6.0	2.1	0.04
LACA	293.1487	−32.8807	−1.3	1.9	−1.5	1.9	−0.03
LEON	290.7029	−31.7989	8.9	1.9	4.8	1.9	−0.02
LICA	294.3146	−38.0802	−2.3	1.9	−3.0	2.1	−0.04
LINC	287.5962	−40.6233	−8.2	2.2	−2.2	2.2	0.08
LISL	288.9890	−31.0609	15.7	1.9	5.5	1.9	−0.02
LMOL	289.5423	−30.7420	11.6	2.1	5.3	1.9	−0.03
LOCE	292.7466	−36.3588	−2.1	1.9	−0.3	2.0	−0.02
LOCO	295.6518	−32.3718	−0.9	1.9	0.6	1.9	−0.05
MARA	292.6712	−31.4553	−2.5	1.9	−0.6	1.9	−0.04
MATA	288.1174	−33.9640	21.9	2.0	8.5	1.9	0.02

Table 1 (*continued*)

Station ID	Longitude	Latitude	W–E vel. (mm/yr)	1σ error	S–N vel. (mm/yr)	1σ error	Correl. coeff.
MAUL	288.2949	−35.5295	27.6	2.0	7.0	2.0	0.04
NEUQ	287.0934	−36.5811	30.8	2.1	8.1	2.0	0.06
NISU	288.0998	−36.2919	21.8	2.0	−1.7	2.0	0.05
OROC	289.2650	−34.2166	13.1	1.9	5.1	1.9	0.01
PANE	290.1747	−30.1928	10.9	1.9	−0.8	1.9	−0.04
PAST	288.5272	−39.5835	−3.4	2.0	−0.4	2.1	0.08
PEHO	288.9261	−38.5967	−3.0	1.9	−5.0	2.1	0.06
PNAZ[a]	289.3463	−26.1482	22.6	1.9	5.7	1.9	−0.07
PPUY	288.0646	−40.7007	0.3	2.0	2.2	2.2	0.10
PSAA	286.5942	−38.7788	19.5	2.0	8.1	2.1	0.10
PTMT	287.0523	−41.4628	−0.6	1.9	4.8	2.2	0.14
PTOM	288.4277	−31.5321	22.6	2.0	6.0	1.9	−0.01
PUAW	287.6075	−38.3383	2.9	2.1	2.3	2.1	0.05
PUCA	286.2800	−40.5468	27.6	2.0	8.5	2.2	0.13
RALU	287.6879	−41.3785	0.6	2.0	3.3	2.2	0.12
RECO	294.9481	−29.2746	−1.4	1.9	4.2	1.9	−0.04
RIPU	292.3534	−28.4312	1.9	1.9	0.0	1.9	−0.04
SANJ	294.6438	−26.7638	−2.1	1.9	1.3	1.9	−0.03
SIAR	293.3291	−31.1641	−1.4	1.9	−0.3	1.9	−0.04
SITI	300.8726	−37.3786	0.4	2.0	0.8	2.0	−0.15
SIVE	298.1999	−38.1375	3.7	1.9	−0.6	2.0	−0.12
SMAR	290.7481	−27.0702	7.2	2.0	5.0	1.9	−0.06
TAFI[a]	294.2190	−26.7444	−3.2	1.9	0.3	1.9	−0.03
TONG	288.4977	−30.2495	13.4	1.9	3.6	1.9	−0.03
TREL	294.6217	−43.2643	−2.3	1.8	1.7	2.3	−0.05
USPA	290.7033	−32.5312	6.2	1.9	3.7	1.9	−0.01
VIMA	296.2764	−29.9136	−5.0	1.9	−2.0	1.9	−0.04
ZAPA	288.5302	−32.5523	19.1	2.0	10.3	1.9	−0.00
1995–1996 campaigns							
BAQU	290.2194	−23.3418	−8.7	4.7	1.5	4.1	0.10
CALC	289.4676	−24.2642	21.0	4.2	6.4	4.1	0.13
CARI	289.5011	−24.9472	18.3	4.3	12.8	4.1	0.15
COBA	290.4112	−24.8242	−9.0	4.3	17.1	4.2	0.14
ESIM	291.1020	−24.2260	−5.4	2.0	15.4	1.9	0.14
JULO	289.4538	−23.5263	24.6	4.8	7.2	4.1	0.11
LHER	290.9397	−25.2232	3.2	4.2	14.0	4.2	0.14
LIVE	289.7471	−23.9642	−1.2	4.2	6.2	4.1	0.12
MINF	290.3942	−24.1048	0.3	4.2	12.7	4.1	0.12
PAEL	290.9586	−23.5383	−24.1	4.1	10.3	4.1	0.11
PASO	291.7093	−24.4492	−1.6	3.9	5.7	4.1	0.13
PCUA	289.7236	−22.6022	1.9	4.2	6.9	4.1	0.09
PENI	291.6541	−23.6400	−10.8	2.1	1.3	2.0	0.08
TALT	289.4905	−25.3998	6.0	4.2	19.3	4.2	0.15
TOPI	289.8064	−22.0338	4.3	4.3	1.5	4.1	0.08
URIB	289.7202	−23.5046	4.1	4.2	11.7	4.1	0.11

[a] These sites were established as part of the Central Andes GPS Project (CAP) [8].

Nazca plate consists of four steep and flat alternating segments, with three transition zones in between [3,4]. Two of these transition zones fall within our study area. Several other tectonic features of the ASZ also exhibit significant along-strike variations that can be related to the geometry of the subducting slab: for example, late Cenozoic magmatic centers are found mostly above steep portions of the subducting slab [1,3]. Contrary to volcanism, earthquakes within the over-

riding South America plate are clustered above flat segments of the slab [5]. Also, the seismicity is considerably low in the fore-arc as compared to the magmatic arc and the back-arc. It is noteworthy to mention that south of 33.5°S latitude, where the dip of the subducting slab steepens, the back-arc seismicity terminates abruptly [6].

Several projects study the present-day deformation of the Central Andes using space geodetic techniques. Norabuena et al. [7] presented for the first time the crustal velocity field in Peru and Bolivia based on GPS measurements. Bevis et al. [8] observed 12 geodetic sites mainly in the Chilean fore-arc north of 22°S. The study filled the existing gap north and south of the Arica deflection. Bevis et al. [8] pointed out the difficulties in combining different GPS solutions. Klotz et al. [9] presented the velocity field between 22°S and 26°S which was strongly affected by the 1995 Antofagasta earthquake. Here we present the contemporary crustal deformation field south of this area which has been until now unknown. In addition we will show the results of a re-survey in the Antofagasta area after the earthquake.

2. Data

Starting in 1993 the GeoForschungsZentrum Potsdam (GFZ), within the framework of South American Geodynamic Activities (SAGA) project and in cooperation with numerous host organizations, has established a large-scale GPS network (more than 200 sites) in Chile and western Argentina. The results presented in this study are based on three GPS campaigns conducted in 1995 and 1996 in the northern section and in 1994 and 1996 in the central and southern sections (Table 1). Each site was observed for at least three consecutive days with daily observation periods of more than 20 h. We used the GFZ processing software EPOS [10] to estimate site coordinates and velocities. The processing was done in three steps. In the *first* step, in order to obtain fiducial-free station coordinates, the campaign data together with the data from IGS global sites and the GFZ South American permanent stations were processed using the IGS combined satellite orbits and Earth orientation parameters. In the *second* step, this solution was transformed to global International Terrestrial Reference Frame (ITRF97). Since the absolute velocities derived within a global reference frame are less precise than those derived for a regional frame, in the *third* step we transformed the ITRF97 solution to a fixed South America reference frame. This transformation was done by estimating a best fitting Euler vector for the South America plate using a least squares adjustment approach and the ITRF97 velocities for five IGS stations located on a stable part of the South America plate. The achieved network precision was derived using the mean value of the position residuals of the IGS stations which were included in the calculation. It ranges between 2 and 4 mm and 5 and 7 mm for horizontal and vertical components, respectively. Since the expected rates of vertical uplift in the ASZ do not exceed 2 mm/yr [11], 2 yr of observations with the above stated vertical precision is not sufficient to resolve these motions with an adequate confidence. For this reason we concentrate further discussion solely on the horizontal deformation rates.

3. Results and discussion

The main finding of our study is shown in Fig. 1 where the contemporary crustal deformation field along the Andean subduction zone between latitudes 22°S and 42°S is depicted in form of velocity vectors. The *two* most prominent features are: (1) The velocity vectors in the central part of the study area (26–37°S), between the coastal towns of Taltal and Concepcion, are high (up to 3.5 cm/yr) and roughly parallel to the relative convergence direction of Nazca and South America plates. Their rate decreases gradually away from the trench. (2) The velocity vectors in the northern (22–26°S) and southern (37–42°S) sections of the study area are oriented in a very non-uniform fashion. We explain both of the above features by the presence of different phases of the earthquake deformation cycle [12]. The observed velocities in the central section represent *interseismic* strain accumulation due to the 100%

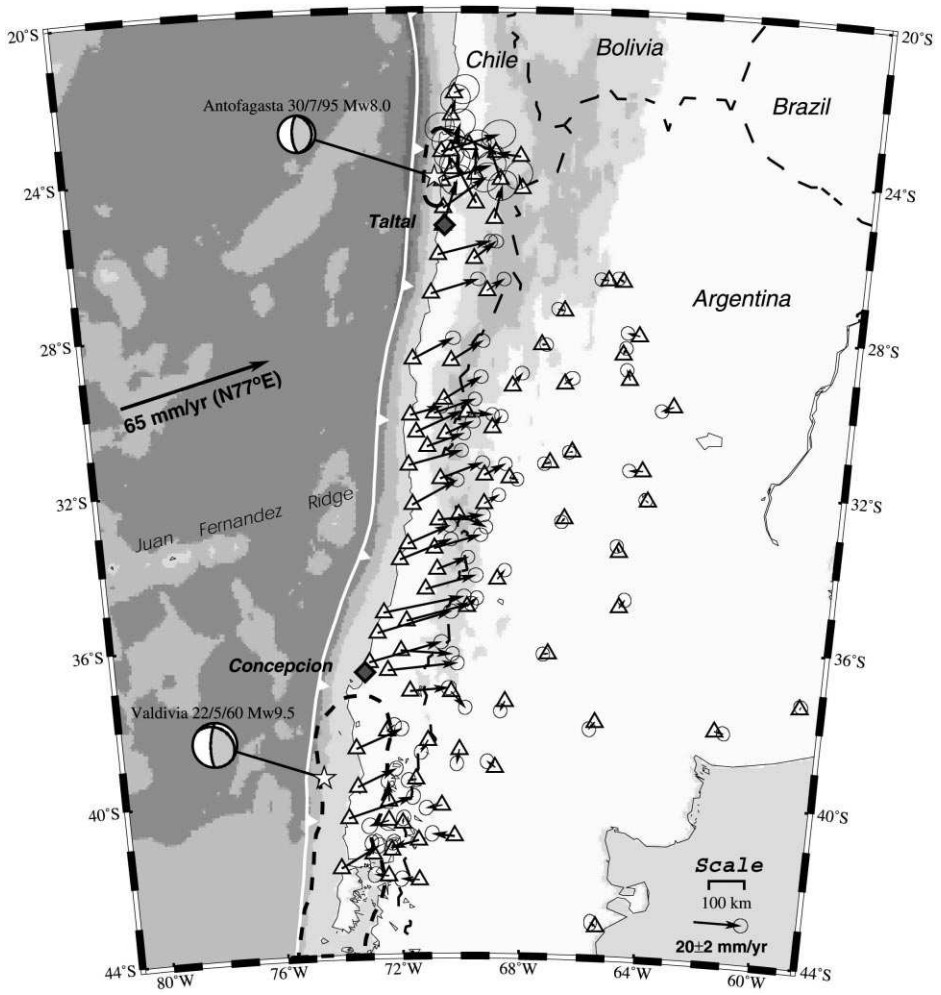

Fig. 1. Map of SAGA GPS network velocities relative to stable South America from 1994–1996 campaigns. Ellipses represent 95% confidence limits. The epicenters and the coseismic rupture areas (dashed lines) of 1995 M_w8.0 Antofagasta [27] and 1960 M_w9.5 Valdivia [28] earthquakes (stars) are shown. Relative convergence vector between the Nazca and South America plates equals 65 mm/yr [17].

locking of the thrust interface between the subducting Nazca and the overriding South America plates.

This interpretation comes from our three-dimensional forward dislocation modeling results. The geometry of our preferred model, called the Andean elastic dislocation model (AEDM) is shown in Fig. 2. To calculate deformation rates predicted by the AEDM at a given set of GPS stations we used a modified version of the program DISL3D, by Kelin Wang of the Pacific Geoscience Centre, Canada. The initial development of this program is attributed to Flück [13,14]. The main principle of the model (and the code) is based on Okada's [15,16] formulation for dislocations in an elastic half-space due to a point source force applied to an infinitesimal surface area. The final goal of estimating deformation rates on the surface of the earth is achieved by dividing the fault surface along the thrust interface (shown as quadrilateral elements in Fig. 2) into 257 600 small triangular elements (each with an area of $\sim$1 km^2) and performing summation for all of the triangles. This approach enables us to intro-

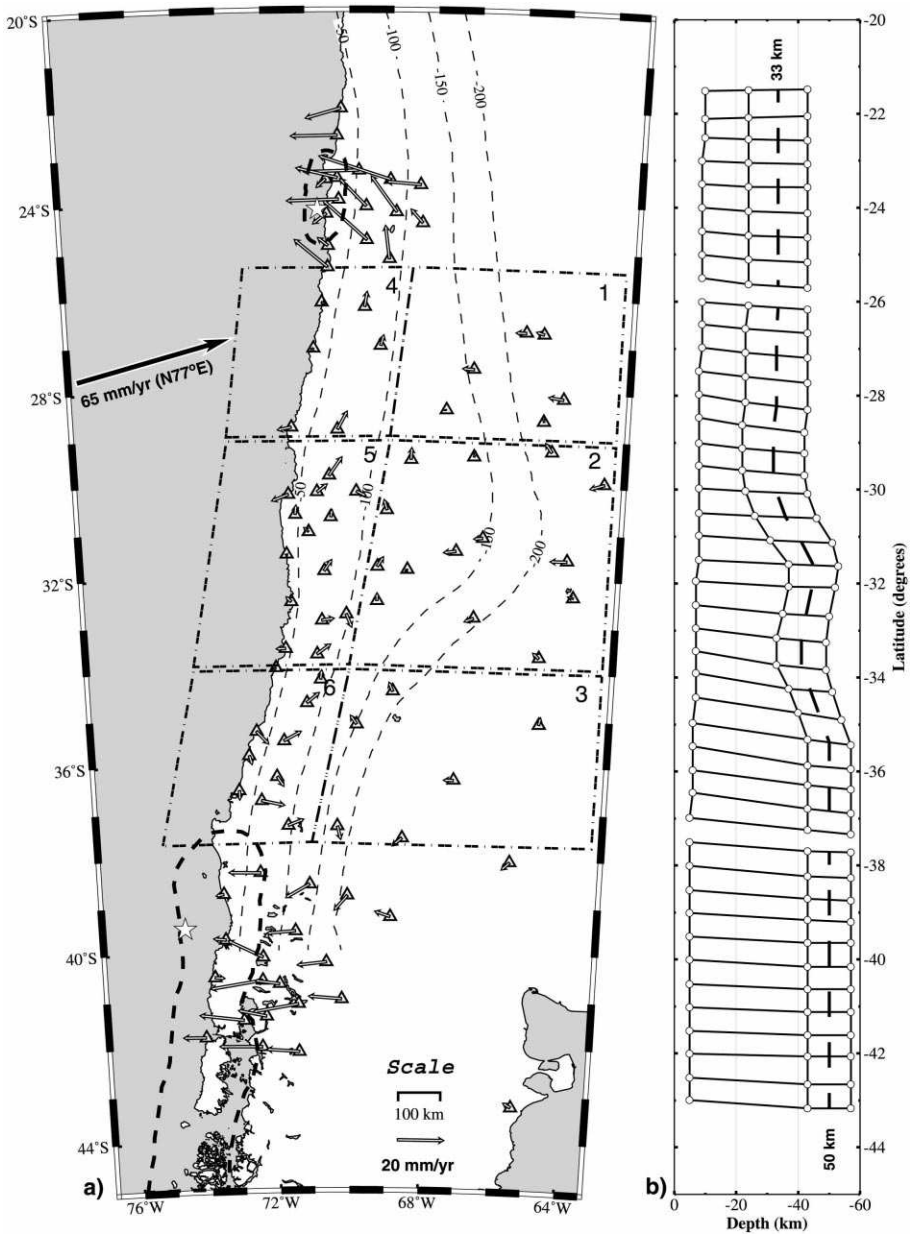

Fig. 2. Seismogenic zone along the Nazca/South America thrust interface deduced from elastic dislocation modeling. (a) Map of residual velocities obtained by subtracting the interseismic signal predicted by the model from the observed velocities. The grid with nodal points depicts the outline of the locked (dark shaded region) and the transition (light shaded region) zones. Dashed contour lines represent the depth to the subducting Nazca slab estimated from Wadati–Benioff zone seismicity [3,4]. Zones 1–6 were used to analyze lateral and longitudinal variability in the residual field. (b) North–south cross-section of the seismogenic zone. The dashed line in the middle of the transition zone shows the average depth extent of geodetically estimated coupling.

duce a curved down-dip profile as is the case within our study area. The two main input parameters that were held fixed throughout the modeling procedure were: (1) the geometry of the thrust interface derived from the location of the trench and the Wadati–Benioff seismicity [3,4]; (2) the assigned slip on the fault was equal to the full plate convergence rate derived from the analysis of GPS data from the stations located on the Nazca and the South American plates [17]. The elastic half-space was described with a Poisson's ratio of 0.25. The unknown parameter that we attempt to estimate through our modeling is the depth of the seismic coupling, represented by the locked and transition zones (shown as dark and light shaded regions in Fig. 2a). The latter is defined as a zone where the fault slip increases linearly from zero at the up-dip end to the plate convergence rate of the steady state subduction at the down-dip end. The inclusion of the transition zone eliminates the possibility of an abrupt discontinuity at the down-dip end of the locked zone which is physically unrealistic [18].

The geodetically estimated depth of coupling (that equals the width of the locked zone plus half of the width of the transition zone) increases from $\sim$33 km depth in the north to $\sim$50 km depth in the south (Fig. 2b). This depth range agrees well with the maximum depth of seismic coupling deduced from the distribution of interplate earthquakes along the ASZ [19], and with the depth of seismogenic zone estimated from thermal modeling [20]. The fact that the transition from the shallow to the deep coupling depth in our model predictions (between latitudes 30°S and 35°S) coincides with the area where the slab becomes steeper, suggests that the deeper portions of the slab might affect the depth of coupling. Earlier studies have uncovered the intriguing coincidence between the changing dip of the slab at 33°S and the place where the Juan Fernandez ridge intersects with the Chile trench [5]. In addition, approximately at the same latitude, two interesting features are observed: (1) an abrupt termination of the back-arc seismicity [6]; (2) a drastic increase in the thickness of the incoming sediment, caused by the change in the climate environment [21].

We attribute the seemingly random orientation of the observed velocity vectors in the northern and southern parts of our study area (Fig. 1) to the continued effects of the past earthquakes. Indeed, when we eliminate the dominant interseismic loading signal from the observed velocities by subtracting the elastic dislocation model predictions, the remaining residual velocity field shows considerably more coherent motion than the initial velocities.

Here we have to note that due to superposition of interseismic and postseismic signals in these areas, we had to assume that the depth of the seismogenic zone was similar to the one estimated for the respective sides of the central section, where the observations are not contaminated by the postseismic effects. Thus, the depth of coupling in the northern and southern sections represents an extrapolation of the AEDM geometry obtained for the central section that results in constant depth of coupling (Fig. 2).

The majority of residual vectors are oriented towards the trench, opposite to the plate convergence direction (Fig. 2a). We interpret the motions detected in the north as the postseismic effects following the 1995 M_w8.0 Antofagasta earthquake. To attribute the deformations observed in the south to the postseismic effects of 1960 M_w9.5 Valdivia earthquake, 35 yr after its occurrence is more astounding. However, if we take into account the fact that this event is the largest earthquake ever recorded in the world, the likelihood of continuing effect of the earthquake becomes more plausible. Our supposition is further re-enforced by recent findings in the western Kenai Peninsula along the Aleutian subduction zone, where GPS observations reveal similar postseismic effects associated with 1964 M_w9.2 Alaska earthquake [22]. Interestingly, recently published 3D viscoelastic deformation modeling results for the Cascadia subduction zone show similar deformation pattern as observed in our study area [23].

Postseismic displacements can be explained either by continuing slip along the deeper (or shallower) sections of the coseismic rupture surface (i.e. afterslip) and/or by viscoelastic relaxation processes occurring within the lower crust and the upper mantle [24]. The former mechanism is

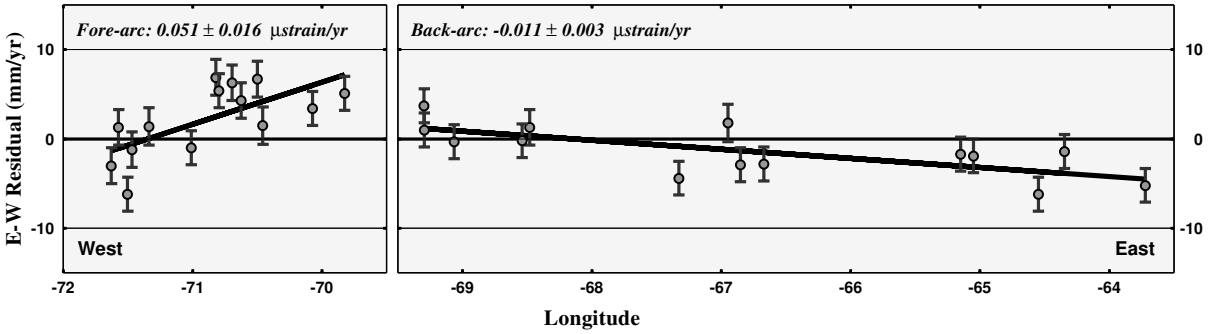

Fig. 3. Long-term deformation signal based on the residual velocities obtained by subtracting the elastic dislocation model predictions from the observed velocities. East components for the sites of zones 2 and 5 (Fig. 2) located within the fore-arc and within the back-arc. Uncertainties are given at 1σ level.

believed to have a more short-term effect, while the latter is generally characterized by more long-term effects. Thus, the deformation in the northern section is most likely due to a continuing afterslip a year after the earthquake, while the viscoelastic relaxation effect is most likely responsible for the movements observed in the south. However, it is difficult to uniquely resolve the relative contribution of the two processes [25].

In addition to isolating the postseismic signal, the subtraction of interseismic signal from raw GPS observations provides means for detecting possible long-term tectonic deformations occurring within the subduction zone. In order to examine a possible north–south variation, we divided the area that is not affected by postseismic relaxation processes into three segments. Each of these segments is again divided by the magmatic arc into fore-arc and back-arc zones (Fig. 2a). Then we examined the north–south and the east–west components of the residual velocities of each zone. A significant signal was only found in the east–west components of zones 2 and 5 (Fig. 3). The presence of a long-term deformation signal within the back-arc is significant: the negative slope of -0.011 ± 0.003 μstrain/yr corresponds to $\sim$6 mm/yr east–west shortening over the distance of 550 km. This result falls within the range of 2–7 mm/yr shortening rate estimated from geological observations spanning the last 25 Ma [26] and gives preference to the higher rate. The positive slope in the east–west components of residual velocities in the fore-arc shown in Fig. 3 indicates a long-term extension within the Chilean fore-arc. However, this finding has to be interpreted with caution since possible modeling uncertainties of large interseismic vectors in the fore-arc are included in the residual velocities.

Finally, the results of our study suggest that all of the plate convergence along the Chilean trench is currently accommodated by the build-up of elastic strain which leads to a high probability of future earthquakes in this region. In order to estimate crudely the possible size of such events, we divided our study area into two $\sim$1000 km long sections, separated by the 32°S parallel where the transition from shallow to deep coupling takes place. Assuming that all of the stored interseismic elastic strain is released during a single thrust earthquake with a repeat time of $\sim$100 yr, the calculated maximum possible magnitude of the hypothetical earthquakes in the northern and southern sections equals M_w9.0 and M_w9.1, respectively. The insignificant difference between the two estimates shows that the variable depth of locking does not have a direct effect on the size of the possible earthquakes, due to the logarithmic relationship between magnitude and fault rupture area. However, the increased depth of coupling results in an overlap of the locked zone with coastal areas south of 35°S (Fig. 2a), that can cause higher levels of ground shaking during the earthquake. This implies an increased seismic hazard to the populated coastal areas, including Concepcion, the second largest city in Chile.

Acknowledgements

This work was supported by the 'GeoForschungsZentrum Potsdam' and by the SFB 267 'Deformationsprozesse in den Anden' of the 'Deutsche Forschungsgemeinschaft'. We are grateful to many organizations and individuals who contributed to the acquisition of the GPS data. Our special thanks go to: Sergio Barrientos, Rodrigo Barriga, Rodrigo Maturana, Victor Hugo Rios and Hansjuergen Haar. We thank Kelin Wang and Paul Flück for the computer code used in 3D dislocation modeling. We are thankful to Tony Qamar and John Castle for thoughtful reviews, as well as Michael Bevis, Eric Kendrick and Robert Smalley Jr. for fruitful cooperation. *[AC]*

References

[1] D. Whitman, B.L. Isacks, S.M. Kay, Lithospheric structure and along-strike segmentation of the Central Andean Plateau; seismic Q, magmatism, flexure, topography and tectonics, Tectonophysics 259 (1996) 29–40.

[2] J. Kley, C.R. Monaldi, J.A. Salfity, Along-strike segmentation of the Andean foreland; causes and consequences, Tectonophysics 301 (1999) 75–94.

[3] T. Cahill, B.L. Isacks, Seismicity and shape of the subducted Nazca Plate, J. Geophys. Res. 97 (1992) 17503–17529.

[4] K.C. Creager, C. Ling Yun, J.P. Winchester, E.R. Engdahl, Membrane strain rates in the subducting plate beneath South America, Geophys. Res. Lett. 22 (1995) 2321–2324.

[5] T.E. Jordan, B.L. Isacks, R.W. Allmendinger, J.A. Brewer, V.A. Ramos, C.J. Ando, Andean tectonics related to geometry of subducted Nazca Plate, Geol. Soc. Am. Bull. 94 (1983) 341–361.

[6] D.S. Chinn, B.L. Isacks, Accurate source depths and focal mechanisms of shallow earthquakes in western South America and in the New Hebrides island arc, Tectonics 2 (1983) 529–563.

[7] E. Norabuena, L. Leffler-Griffin, A. Mao, T. Dixon, S. Stein, S.I. Sacks, L. Ocola, M. Ellis, Space geodetic observations of Nazca-South America convergence across the central Andes, Science 279 (1998) 358–362.

[8] M. Bevis, E.C. Kendrick, R. Smalley Jr., T. Herring, J. Godoy, F. Galban, Crustal motion north and south of the Arica deflection; comparing recent geodetic results from the Central Andes, G3 1 (1999) 1–12.

[9] J. Klotz, D. Angermann, G.W. Michel, R. Porth, C. Reigber, J. Reinking, J. Viramonte, R. Perdomo, V.H. Rios, S. Barrientos, R. Barriga, O. Cifuentes, GPS-derived deformation of the Central Andes including the 1995 Antofagasta M (sub w) = 8.0 earthquake, Pure Appl. Geophys. 154 (1999) 3709–3730.

[10] D. Angermann, G. Baustert, R. Galas, S.Y. Zhu, EPOS.P.V3 (Earth Parameter and Orbit System): Software User Manual for GPS Data Processing, in: Scientific Technical Report STR97/14, GeoForschungsZentrum, Potsdam, 1997, p. 52.

[11] T.E. Jordan, J.H. Reynolds, III, J.P. Erikson, Variability in age of initial shortening and uplift in the Central Andes, in: F. Ruddiman-William (Ed.), Tectonic Uplift and Climate Change, Plenum Press, New York, 1997, pp. 41–61.

[12] W. Thatcher, Cyclic deformation related to great earthquakes at plate boundaries, Bull. R. Soc. N. Zealand 24 (1986) 245–272.

[13] P. Flück, 3-D dislocation model for great earthquakes of the Cascadia subduction zone, diploma, Swiss Federal Institute of Technology (ETH), 1996.

[14] P. Flück, R.D. Hyndman, K. Wang, Three-dimensional dislocation model for great earthquakes of the Cascadia subduction zone, J. Geophys. Res. 102 (1997) 20539–20550.

[15] Y. Okada, Surface deformation due to shear and tensile faults in a half-space, Bull. Seismol. Soc. Am. 75 (1985) 1135–1154.

[16] Y. Okada, Internal deformation due to shear and tensile faults in a half-space, Bull. Seismol. Soc. Am. 82 (1992) 1018–1040.

[17] D. Angermann, J. Klotz, C. Reigber, Space-geodetic estimation of the Nazca–South America Euler vector, Earth Planet. Sci. Lett. 171 (1999) 329–334.

[18] H. Dragert, R.D. Hyndman, G.C. Rogers, K. Wang, Current deformation and the width of the seismogenic zone of the northern Cascadia subduction thrust, J. Geophys. Res. 99 (1994) 653–668.

[19] B.W. Tichelaar, L.J. Ruff, Seismic coupling along the Chilean subduction zone, J. Geophys. Res. 96 (1991) 11997–12022.

[20] D.A. Oleskevich, R.D. Hyndman, K. Wang, The updip and downdip limits to great subduction earthquakes: Thermal and structural models of Cascadia, south Alaska, SW Japan, and Chile, J. Geophys. Res. 104 (1999) 14965–14992.

[21] N.L. Bangs, S.C. Cande, Episodic development of a convergent margin inferred from structures and processes along the southern Chile margin, Tectonics 16 (1997) 489–503.

[22] J.T. Freymueller, S.C. Cohen, H.J. Fletcher, Spatial variations in present-day deformation, Kenai Peninsula, Alaska, and their implications, J. Geophys. Res. 105 (2000) 8079–8101.

[23] K. Wang, J. He, H. Dragert, T. James, Three-dimensional viscoelastic interseismic deformation model for the Cascadia subduction zone, Earth Planet. Space 53 (2001) 295–306.

[24] S.C. Cohen, Numerical models of crustal deformation in seismic zones, in: R. Dmowska, B. Saltzman (Eds.), Advances in Geophysics Vol. 41, Academic Press, New York, 1999, pp. 133–231.
[25] F.F. Pollitz, R. Burgmann, P. Segall, Joint estimation of afterslip rate and postseismic relaxation following the 1989 Loma Prieta earthquake, J. Geophys. Res. 103 (1998) 26975–26992.
[26] J. Kley, C.R. Monaldi, Tectonic shortening and crustal thickness in the Central Andes; how good is the correlation?, Geology 26 (1998) 723–726.
[27] B. Delouis, H. Philip, L. Dorbath, A. Cisternas, Recent crustal deformation in the Antofagasta region (northern Chile) and the subduction process, Geophys. J. Int. 132 (1998) 302–338.
[28] G. Plafker, Alaskan Earthquake of 1964 and Chilean Earthquake of 1960; implications for Arc Tectonics, J. Geophys. Res. 77 (1972) 901–925.